Pulsed Laser Deposited Fe_2TiO_5 Photoanodes for Photoelectrochemical Water Oxidation

Prince Saurabh Bassi[†]*, Fanxing Xi[†], Moritz Kölbach[†], Rene Gunder[§], Ibbi Ahmet[†], Roel van de Krol[†‡], Sebastian Fiechter[†]*

[†] Institute for Solar Fuels, Helmholtz-Zentrum Berlin für Materialien und Energie GmbH, 14109 Berlin, Germany

[§] Structure and Dynamics of Energy Materials, Helmholtz-Zentrum Berlin für Materialien und Energie GmbH, 14109 Berlin, Germany

[‡] Institut für Chemie, Technische Universität Berlin, Straße des 17. Juni 124, 10623 Berlin, Germany

Keywords: Solar energy conversion, light-driven water oxidation, ternary transition metal oxide electrode, oxygen atmosphere, nanoporous film

ABSTRACT

Pulsed laser deposition (PLD) is an appealing technique to fabricate thin films with specific film orientation, stoichiometry, and morphology through tuning of experimental parameters. Here, we present Fe_2TiO_5, one of the promising photoanode materials, grown on fluorine-doped tin oxide (FTO) substrates through PLD. The structural and morphological properties of Fe_2TiO_5 films, grown at room temperature and under varying oxygen pressure were studied. After deposition, all films were annealed in air at 650°C for 2 hours to complete phase crystallization. Films grown under vacuum (1.1×10^{-6} mbar) were compact, dense, and had the anticipated stoichiometry, but lacked the long-range order expected for a crystalline phase in X-ray diffraction. In contrast, using an oxygen pressure (p_{O_2}) of around 9.7×10^{-2} mbar during growth resulted in nanoporous, crystalline, and near-stoichiometric films of the orthorhombic Fe_2TiO_5 pseudobrookite phase. These films demonstrated a photocurrent density of around 0.16 mA/cm^2 at 1.23 V vs RHE and a negative shift in onset potential by 150 mV under backside illumination as compared to the films grown under vacuum. Notably, these films exhibited a preferred (101) orientation of the pseudobrookite grains. This study proposes a viable strategy to fabricate pure phase and anisotropic Fe_2TiO_5 photoanodes on FTO through PLD. This will pave a way to synthesis of other complex metal oxide photoelectrodes with precise control over critical properties like crystallinity, stoichiometry, and porosity that is imperative for their application in solar energy conversion.

INTRODUCTION

Impending rise in energy demand due to the rapid evolution of technology along with the social and economic development of a growing population has led to climate change concerns due to the colossal burning of fossil fuels. Among alternative energy sources, solar energy is by far the most abundant source and is hence crucial to mitigate climate change and to limit global warming to below 2°C.[1-2] However, its intermittent nature restricts its utility as an energy source. To address this limitation, direct photoelectrochemical water splitting can be used to directly convert solar energy into chemical bonds, the products of which can be stored indefinitely and transported efficiently. When immersed in an electrolyte, certain semiconducting photoelectrodes can split water into hydrogen and oxygen under illumination. Under the right conditions, an n-type semiconducting photoanode can evolve oxygen on its surface while hydrogen, a clean fuel, is produced at the counter electrode (cathode side).[3] But the stringent criteria for an efficient photoelectrocatalyst, such as thermodynamic stability under operating conditions in the electrolyte, an optimum bandgap in the range from 1.6 to 2 eV to achieve high efficiencies, a high mobility of excited electrons and holes, and fast oxygen and hydrogen evolution kinetics have thus far limited the prospects of commercial development of photoelectrochemical cells. A lot of research has been done on binary metal oxides such as Fe_2O_3, TiO_2, WO_3, etc. as photoanodes but the large bandgaps of TiO_2 and WO_3 restrict the efficiency they can achieve whereas Fe_2O_3 is limited by its charge transport.[4-8] In that context, research on mixed metal oxides especially ternary oxides such as $BiVO_4$, $SnWO_4$, $SnNb_2O_6$, $BaSnO_{3-\delta}$, $Cu_2V_2O_7$, etc. has proven promising.[9-15] Among those, Fe_2TiO_5 is relatively less explored and has gained attention over a couple of years, due to its bandgap of 2.1 eV and high electrochemical and thermodynamic stability.[16-17] The fabrication of pure phase Fe_2TiO_5 photoanodes through solvothermal synthesis and extraction of its band levels by ultraviolet photoelectron spectroscopy (UPS) and X-ray photoelectron spectroscopy (XPS), was reported earlier by one of the authors.[18] Synthesis of Fe_2TiO_5 through systematic doping of Fe in the TiO_2 lattice was demonstrated by Courtin *et al*.[19] Thin film

deposition using a template has also been reported where nano/microstructures resulted in enhanced light absorption and hence better photoactivity of the Fe_2TiO_5 absorber layers.[20-21] Besides, heterostructures of Fe_2TiO_5 with Fe_2O_3 and TiO_2, owing to the favorable band alignment it forms with these oxides, have also been presented.[22-25] One of such earliest accounts was the usage of TiO_2 nanotube arrays deposited on a Ti substrate with a Fe_2TiO_5 conformal layer on top, where the latter worked as an absorber and the former as the charge transport facilitating material.[26] Other reports on coupling Fe_2O_3 and Fe_2TiO_5 also gained significant attention.[27-31] We also reported on crystalline heterojunction Fe_2O_3/Fe_2TiO_5 based nanorods which yielded significant enhancement in the performance due to favorable charge separation through a type-II band alignment.[32] But most of the work has concentrated on the synthesis of films using solvothermal processes which are known to yield films with strain, defects, and highly structured/porous morphologies. This makes it difficult to study such films. There has been a need to fabricate thin, compact films with better-defined composition and a higher degree of crystallinity. For this, physical vapor deposition methods like Pulsed Laser Deposition (PLD) has proven to be effective. This technique to deposit Fe_2TiO_5 films has not been explored in-depth yet. In principle, laser pulses vaporize a stoichiometric pellet (called a 'target') creating a plume of ions that condense on the substrate. This allows nucleation and growth of the film on a substrate with characteristics that depend on working pressure, laser fluence, target to substrate distance, repetition rate and substrate temperature.[33-34] Recently, Osada *et al.* reported epitaxial films of Fe_2TiO_5 deposited on $LaAlO_3$ (001)-oriented substrates and investigated their optical and electronic properties.[35] They found that the room temperature resistivity was in the range from 20 to 80 Ωcm, significantly lower than the values reported for Fe_2O_3. Stabilization of (100) and (230) oriented films by controlling oxygen partial pressure and temperature during deposition was also reported. Ngo *et al.* demonstrated the synthesis of pseudobrookite Fe_2TiO_5 thin films with RF magnetron sputtering.[36] These films deposited on glass and silicon substrates were characterized for their chemical composition, crystal structure, surface morphology, and optical properties both experimentally and theoretically. The film was confirmed to be a single-phase and preferentially oriented in the orthorhombic [131] direction. These

reports give an overview of the intrinsic properties of Fe_2TiO_5 but none have been used as photoanodes in photoelectrochemical cells. This is, in particular, a different task since the base substrate for photoanodes is generally a transparent and polycrystalline conducting oxide (TCO), like F-doped SnO_2 (FTO) or Sn-doped In_2O_3 (ITO). FTO, in particular, is useful because it provides long term aqueous and thermodynamic stability in aqueous electrolytes. TCOs are also transparent and allow the light to pass through it for complete solar light absorption when coupled with a complementary (lower-bandgap) bottom photoabsorber in tandem devices. Given the nearly optimum bandgap of Fe_2TiO_5 and its high aqueous stability, solar water oxidation of PLD grown films is an interesting area to investigate for its photoelectrochemical properties.

Here, we report the deposition of Fe_2TiO_5 thin films on FTO substrates using the pulsed laser deposition technique through optimization of the oxygen atmosphere in the growth chamber. These films yield photocurrent densities of 0.16 mA/cm^2 and 0.12 mA/cm^2 at 1.23 V vs RHE when deposited under 9.7 x 10^{-2} mbar oxygen pressure and vacuum (1.1 x 10^{-6} mbar), respectively. Films deposited under oxygen atmosphere (9.7 x 10^{-2} mbar) show preferentially (101)-oriented pseudobrookite grains. To the best of our knowledge, this is the first report on anisotropic, crystalline, and near-stoichiometric Fe_2TiO_5 thin films, fabricated on polycrystalline FTO substrates through pulsed laser deposition for application in photoelectrochemical water oxidation.

EXPERIMENTAL SECTION

Details about the Pulsed Laser Deposition process

Thin Fe_2TiO_5 films with a thickness ranging from 50 – 200 nm were deposited on FTO substrates using pulsed laser deposition in a custom-built system (PREVAC, Poland). After deposition, all samples were annealed with an optimized ramping profile in a muffle oven in air at 650°C for 2 hours (2°C/min) for phase crystallization. A KrF excimer laser LPXpro210 (248 nm wavelength, τ = 25 ns, E = 0.7 J), integrated into the system, was used to ablate the rotated and translated lab-prepared target with a laser spot size of 1.3 × 2

mm^2 and a pulse frequency of 10 Hz. A schematic representation of the PLD equipment is shown in Figure S1 (Supporting Information (SI)). A laser fluence rate of 2.5 J/cm^2 was used for all experiments. The FTO substrates were clamped on a substrate holder that was positioned off-axis (12 cm from the central axis of the plume) and rotated at an angular speed of 12° s^{-1} to ensure uniform deposition. No intentional substrate heating was used during deposition. A fixed substrate-to-target distance of 56 mm was used for all the depositions. The vacuum chamber had a background pressure of around 1.1 x 10^{-6} mbar. O_2 gas was introduced in the chamber to tune the working pressure of the chamber, ranging from 1.1 x 10^{-6} to 9.7 x 10^{-2} mbar. Before the deposition, the target was pre-ablated to ensure the stabilization of the deposition rate, measured using a quartz crystal microbalance. The thickness of the films was adjusted through the number of laser pulse cycles and was measured using a Dektak profilometer.

Conditions of PLD target preparation

The Fe_2TiO_5 target was prepared by mixing Fe_2O_3 (99.995% trace metals basis, Sigma Aldrich) and TiO_2 (Puratronic, 99.995% metals basis) powders in a 1:1 molar ratio and milling them using zirconia grinding bowl (400 ml, 50 mm in diameter) under vibration for 1h. The obtained powder was pressed under vacuum into a pellet of 30 mm in diameter and 8 mm thickness (Figure S2a). The pellet was then sintered at 1300°C for 12 hours in the air to crystallize the Fe_2TiO_5 pseudobrookite phase, which was used as the target for film deposition (Figure S2a, SI). The phase crystallinity of the sintered target was confirmed with X-ray diffraction (XRD) (Figure S2b, SI). The Field Emission Scanning Electron Microscopy (FESEM) image of ablated and non-ablated parts of the target are shown in Figure S2c, SI.

Preparation of FTO substrates

Transparent FTO-coated glass pieces (2.5 cm x 2.5 cm x 0.22 cm, TEC 7, Pilkington) were used as conducting electrodes for the deposition of the Fe_2TiO_5 films. Before deposition, the FTO substrates were ultrasonically cleaned thoroughly with a soap solution, followed by rinsing and ultrasonically cleaning in

deionized (DI) water, acetone, ethanol, 1M KOH and finally twice with DI water for 15 min in each solution. As the final step, they were blow-dried using compressed nitrogen flow.

Structural, morphological and optical characterization

The XRD patterns of both the target and the thin films were obtained using a Panalytical X'Pert Pro MPD diffractometer with Cu Kα radiation (λ = 0.15406 nm or 1.5406 Å). For measurements on the target, the Bragg-Brentano geometry was used with a 10° to 70° 2θ range and a 0.01° step size (Figure S2b, SI). For thin films, the measurements were done in grazing incidence geometry with an incident angle of 0.5° and 2θ ranging from 10° to 60° with a step size of 0.04°.

For optical properties, UV vis measurements were performed on thin films via the backside of the glass substrate in an integrating sphere on a Perkin Elmer Spectrophotometer (Lambda 950S). Substrates were placed in a center mount sample holder, oriented in a ~7.5° offset from the incident ray. This yielded the transflectance, which is the sum of the transmittance and reflectance of the films. The absorption (A) and the absorption coefficient (α) were extracted from transflectance (TR) using the following equations:

$$A = - \log_{10} (TR) \quad (1)$$

$$\alpha = 2.303/t * \log_{10}((1-R)/T) \quad (2)$$

where t = effective thickness of the film. The number of cycles during PLD were kept constant to attain a thickness of 100 nm. To calculate the absorption coefficient values, reflectance (R) and transmittance (T) were measured separately and the above expression was used while assuming the influence of FTO substrate to be negligible.

The general relation between incident photon energy ($h\nu$) and the optical band gap energy (E_g) is given as:

$$(\alpha h\nu)^n = C (h\nu - E_g) \quad (3)$$

where C is a constant and n = 1/2 for an indirect and n = 2 for a direct transition. To extract the bandgap for these films, both transitions were evaluated using Tauc plot analysis.

The Fe/Ti-ratio of the films deposited on glassy carbon (5 × 10 mm^2, Sigradur G, HTW) was determined by Rutherford Backscattering Spectrometry (RBS). The spectra of the films were recorded with 1.7 MeV ^4He ions at a detector angle of 170°. The experimental data were fitted with the SIMNRA software.

The morphology of the films and targets was studied using Field Emission Scanning Electron Microscopy (FESEM). An LEO GEMINI 1530 instrument from ZEISS was used for these measurements with an acceleration voltage of 5 kV. For Energy Dispersive X-ray analysis (EDX), an acceleration voltage of 13 kV was used.

X-ray photoemission spectroscopy (XPS) was measured with a home built ultrahigh vacuum system at < 10^{-8} mbar. XPS was performed with a monochromatic Al Kα X-ray-source (1486.74 eV) using a FOCUS 500 X-ray monochromator and a PHOIBOS 100 hemispherical analyser. The source-to-analyzer angle was set at 54°. All high-resolution spectra were measured using a pass energy and step size of 10 and 0.05 eV, respectively. CasaXPS was used for the data processing. To calibrate the peak position, the C 1s peak was fitted to the aliphatic carbon reference of 284.8 eV and the other peak positions where adjusted accordingly. A Shirley background was used for all peak models. The elemental ratios were determined from the total peak areas of the Ti $2p_{3/2}$ and Fe $2p_{3/2}$ peaks divided by the product of the respective relative sensitivity factors (RSF), transmission function of the analyzer (T) and the energy dependent inelastic mean free path (MSF). The relative area calculated from a fitted peak model for the Fe $2p_{3/2}$ region was used to determine ratio of Fe^{3+} to Fe^{2+}. For the Fe $2p_{1/2}$ region, a main peak and broad satellite peak were fitted such their relative areas were half the total peak area of the Fe $2p_{3/2}$ region.

Photoelectrochemical characterization

Photoelectrochemical (PEC) measurements were performed in a custom-made PEC cell using a three-electrode configuration, with the thin Fe_2TiO_5 films as the working electrode, platinum wire as the counter electrode, and an Ag/AgCl reference electrode (Radiometer Analytical, Saturated KCl, 0.197 V vs normal hydrogen electrode). A WACOM solar simulator (WXS-505-5H, Class AAA) with AM 1.5G (1 sun) illumination was used as the light source for photoelectrochemical measurements. The illuminated circular area was around 0.24 cm^2 and the same aperture also defined the area that was in contact with the electrolyte. The electrochemical potential was applied using an EG&G Princeton Applied Research Potentiostat (Model 273A). Photocurrent density was measured in 1M NaOH solution (pH = 13.6) as electrolyte with a potential scan rate of 20 mV s^{-1}. Potentials applied with respect to an Ag/AgCl electrode were converted with respect to reversible hydrogen electrode using Nernst equation ($E_{RHE} = E_{Ag/AgCl} + 0.197$ V + 0.059 V *pH).

Incident photon-to-current efficiency (IPCE) measurements were performed using a Xe lamp (LOT, LSH302) coupled with an Acton Research monochromator (Model: Spectra Pro 2155). The monochromator was used in combination with an electronic shutter (Model: Uniblitz LS6) and a long pass colored filter (Schott glass). The calibration of the light intensity was performed by placing a bare FTO substrate in the PEC cell and measuring the transmitted light with a calibrated photodiode (PD300R-UV, Ophir). The formula for calculating IPCE is as given below:

$$IPCE\ (\lambda) = (1240\ [V\ nm] \times j(\lambda)\ [mA/cm^2]) / (P_{light}(\lambda)\ [mW/cm^2] \times \lambda\ [nm]) \quad (4)$$

Where $j(\lambda)$ is the photocurrent density and $P_{light}(\lambda)$ is the intensity of the monochromator light, at the respective wavelengths λ.

RESULTS AND DISCUSSION

Stoichiometry, structure & morphology

In the PLD process of metal oxides, the film properties (e.g. stoichiometry and crystallinity) mainly depend on the laser fluence, the substrate temperature, and the background gas. In this work, we focus on the effect of oxygen pressure during deposition on the properties of the iron titanate films fabricated from a Fe_2TiO_5 target. The laser fluence and substrate temperature were fixed to 2.5 J/cm^2 and room temperature, respectively, during deposition, and all films were post-deposition annealed at 650°C for 2h in air irrespective of their deposition conditions.

The introduction of oxygen pressure during the deposition can strongly influence the properties of the deposited films.[37] Specifically, the ablated species can collide with the oxygen species, resulting in a shock plume front and a deceleration/thermalization of the plasma front.[38] Since this deceleration of the species can be more pronounced for the lighter cations, deviations from an ideal target-to-substrate material transfer in the PLD process of complex metal oxides can occur. This was, for example, shown for $LiMn_2O_4$[39] and $BiVO_4$ [40], where the deposited films were found to be deficient in the much lighter cations Li and V, respectively, when a sufficiently high oxygen pressure was added. In the case of Fe_2TiO_5, however, such a dependence is not expected since the atomic masses of Fe (u = 55.8) and Ti (u = 47.9) are rather similar. The RBS analysis of films deposited in vacuum (< 1.1 x 10^{-6} mbar), 9.0 x 10^{-3} mbar O_2, and 9.7 x 10^{-2} mbar O_2 shows that cation stoichiometry is indeed not affected by the oxygen pressure in this range (Figure 1). A Fe:Ti ratio of approx. 1.8 ± 0.1 is found for all films. This value is close to the ideal ratio of 2 that is expected for the desired Fe_2TiO_5 phase. The reason for the slight Ti-enrichment and its impact on the film properties is beyond the scope of this work. However, future work can be directed into the optimization of other PLD process parameters like the fluence and the substrate temperature to investigate a possible preferential ablation of Ti from the target or resputtering/reevaporation of Fe from the deposited film.

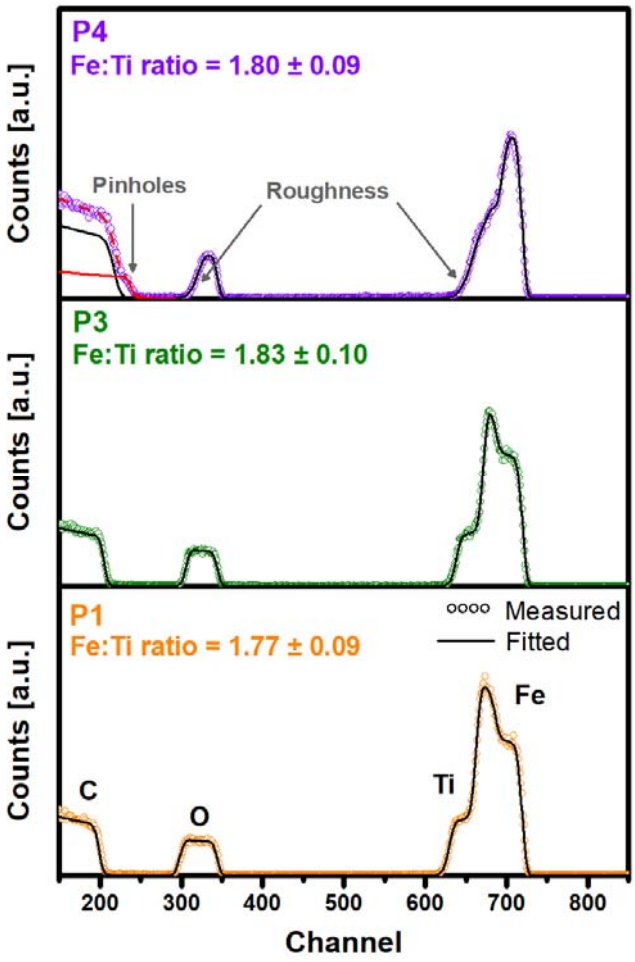

Figure 1: Rutherford Back Scattering (RBS) analysis of films deposited on glassy carbon substrates under vacuum (P1), and under oxygen background pressures of p_{O_2} = 9.0 x 10^{-3} mbar (P3), and p_{O_2} = 9.7 x 10^{-2} mbar (P4).

Besides the stoichiometry, the growth mode and hence the morphology of the deposited films can be influenced by thermalization of the ablated species in an oxygen-containing atmosphere.[41-43] For example, Infortuna *et al*. elucidated the role of background pressure in achieving porous yttrium-stabilized zirconia (YSZ) and cerium gadolinium oxide (CGO) thin films.[42] They conclude that a higher processing pressure impedes the mobility of species and leads to the crystallization of grains, as opposed to the case with low pressure where the atomic rearrangement at the grain boundaries leads to a denser structure. This effect

is also evident with the deposition of Fe_2TiO_5 in an oxygen pressure of 9.7 x 10^{-2} mbar and becomes apparent as a shoulder in the RBS signals, which can only be fitted when the surface roughness is included in the model (marked with arrows in the P4 panel of Figure 1). Also, a mismatch between the measured values and the fit of the carbon signal (substrate) is observed for this film which can be explained as follows. Using $Fe_xTi_yO_z$/C as an input in the model, the fit of the carbon substrate signal is based on $^4He^+$ ions that have lost some of their kinetic energy due to inelastic scattering while traversing the $Fe_xTi_yO_z$ layer. Therefore, the signal of the substrate usually shifts to lower channels (i.e. backscattering energy). The shoulder at higher channels can be fitted when only carbon is used as an input (red line) and is hence a strong indication for pinholes in the film. The sum of both fits is shown as a dashed red line and is in accordance with the measured values. These findings show a clear morphology change of the as-deposited films (i.e. an increase of roughness and pinholes) as the oxygen pressure is increased.

To investigate the phase formation with changing oxygen pressure, grazing incidence X-ray diffraction (XRD) of the annealed films was performed. The obtained diffractograms are presented in Figure 2a. Films deposited at oxygen pressures ranging from 1.1 x 10^{-6} mbar to 9.0 x 10^{-3} mbar show only low-intensity peaks corresponding to the hematite (α-Fe_2O_3) phase (α phase in Figure 2a represented by two peak positions at 2θ ~ 24.5° and 36°). Since the pattern for Fe_2O_3 and Ti-alloyed Fe_2O_3 are quite similar, the exact phase composition present in these films cannot be determined from the XRD alone.[44] The two broad peaks at 2θ ~ 24.5° and 36° can also be assigned to $Fe_{1.698}Ti_{0.228}O_3$ (JCPDS # 04-009-6569) which is possibly a metastable phase before complete crystallization of amorphous films into Fe_2TiO_5 phase occurs. This is also evident from the peak at 2θ ~ 24.5° which diminishes with increasing oxygen pressure. A radical change in the diffractogram was observed for films deposited under an oxygen pressure of 9.7 x 10^{-2} mbar. The sharp diffraction peak at 2θ ~ 25.53° can now be attributed to the Fe_2TiO_5 pseudobrookite phase (JCPDS # 00-041-1432). It shows the growth of the orthorhombic phase with a preferential orientation of the grains with (101) lattice planes parallel to the substrate. Peaks of higher intensities (presented as # in

Figure 2a) originate from the FTO layer underneath the films. We calculated the lattice parameters using the diffraction peaks at 2θ = 18.13°, 25.53°, 36.53°, and 48.81° from the XRD pattern for films deposited at an oxygen pressure of 9.7 x 10^{-2} mbar. The values of lattice constants derived for $Fe_{2-x}Ti_{1+x}O_5$ crystallizing in the orthorhombic space group Cmcm amounted to *a = 3.729 Å* , *b= 9.778 Å* and *c = 9.943 Å*. These values are slightly different from earlier reported ones of *a = 3.732 Å, b = 9.793 Å, c = 9.979 Å*[45] signifying a possibly disordered cationic sublattice due to a smaller c lattice constant. Our findings from RBS and XRD analysis are in agreement with the study of ferric pseudobrookite composition presented by Seitz *et al.*[46] They concluded that "stoichiometric" Fe_2TiO_5 always contains Fe_2O_3 phase and a moderate increase in titanium concentration coupled with an adequate thermal treatment which helps to achieve the pure solid solution. Besides, the formation of Fe_2O_3 or TiO_2 as secondary phases depends on the amount of cationic vacancies created, differing with the film's thermal history.

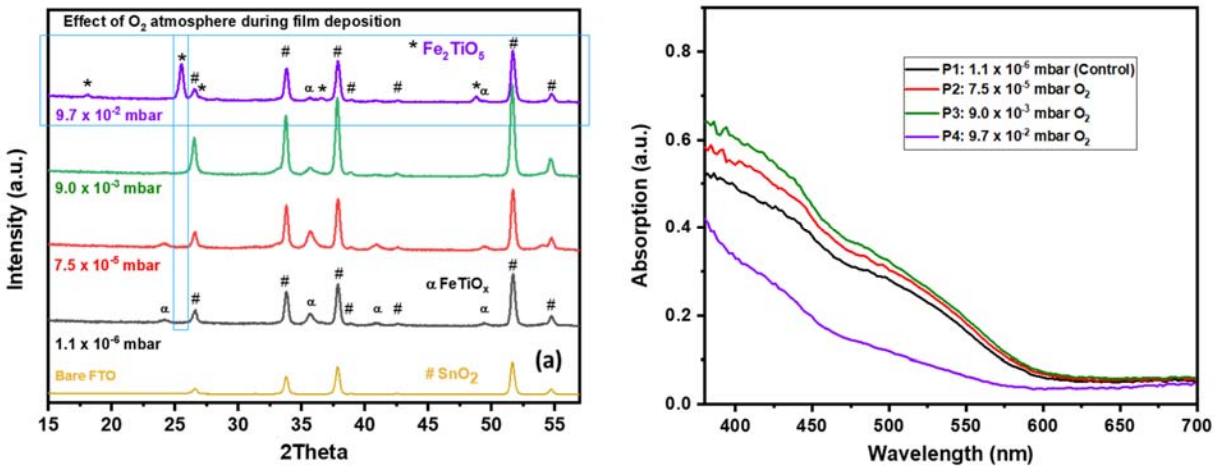

Figure 2: (a) X-Ray Diffraction (XRD) pattern and (b) UV-Vis absorption spectra, for thin films deposited under different background pressures. All the films were annealed at 650°C for 2h in air.

Optical absorption of films deposited under different background pressures was studied using UV-vis spectroscopy. The visible light absorption behavior (shown in Figure 2b) increases with decreasing wavelength for λ < 590 nm. When comparing samples P1 to P4 (deposited at different oxygen pressures),

absorption increases with increasing oxygen pressure from 1.1 x 10^{-6} to 9.0 x 10^{-3} mbar but at higher oxygen pressures a pronounced drop in the absorbance curve was noticed for the P4 sample, i.e. for the film deposited at p_{O_2} = 9.7 x 10^{-2} mbar. From XRD analysis, we know that sample P4 consists of crystalline Fe_2TiO_5, which is known to possess a small absorption coefficient, which correlates with the trend in the absorption curves. This behavior indicates a phase transformation and simultaneous crystallization of annealed films that were deposited at an oxygen pressure of 9.7 x 10^{-2} mbar.

From here on, samples deposited in a pressure condition of 9.7 x 10^{-2} mbar O_2 will be simply referred to as samples deposited in an oxygen atmosphere, whereas the ones deposited in the background pressure of 1.1 x 10^{-6} mbar will be referred to as samples deposited in vacuum.

From the reflectance and transmittance data, the absorption coefficient (α) values were extracted for the films as shown in Figure S3(a), SI. A film thickness of 100 nm was used for this calculation (*vide infra*). Absorption coefficients of around 1.1 x 10^5 cm^{-1} and 4.7 x 10^4 cm^{-1} at 480 nm, were observed for films deposited in vacuum and oxygen atmosphere (9.7 x 10^{-2} mbar), respectively. Hence, films deposited under vacuum absorb considerably more solar light than films grown in an oxygen atmosphere. To evaluate the size and nature of the bandgap, the optical absorption data was represented in Tauc plots (Figure S3(b)) as $(\alpha h\nu)^2$ vs $h\nu$ for direct and $(\alpha h\nu)^{1/2}$ vs $h\nu$ for the indirect transition.[47] For films grown under an oxygen atmosphere, $E_g^{indirect}$ amounts to ~ 2.11 eV and E_g^{direct} to ~ 2.3 eV which closely matches previous reports.[18, 36] Films grown in vacuum showed lower band gaps (indirect - 2.04 eV and direct - 2.18 eV) which could point out the presence of oxygen deficiencies in the lattice, still unchanged after the post-deposition annealing in air.[48]

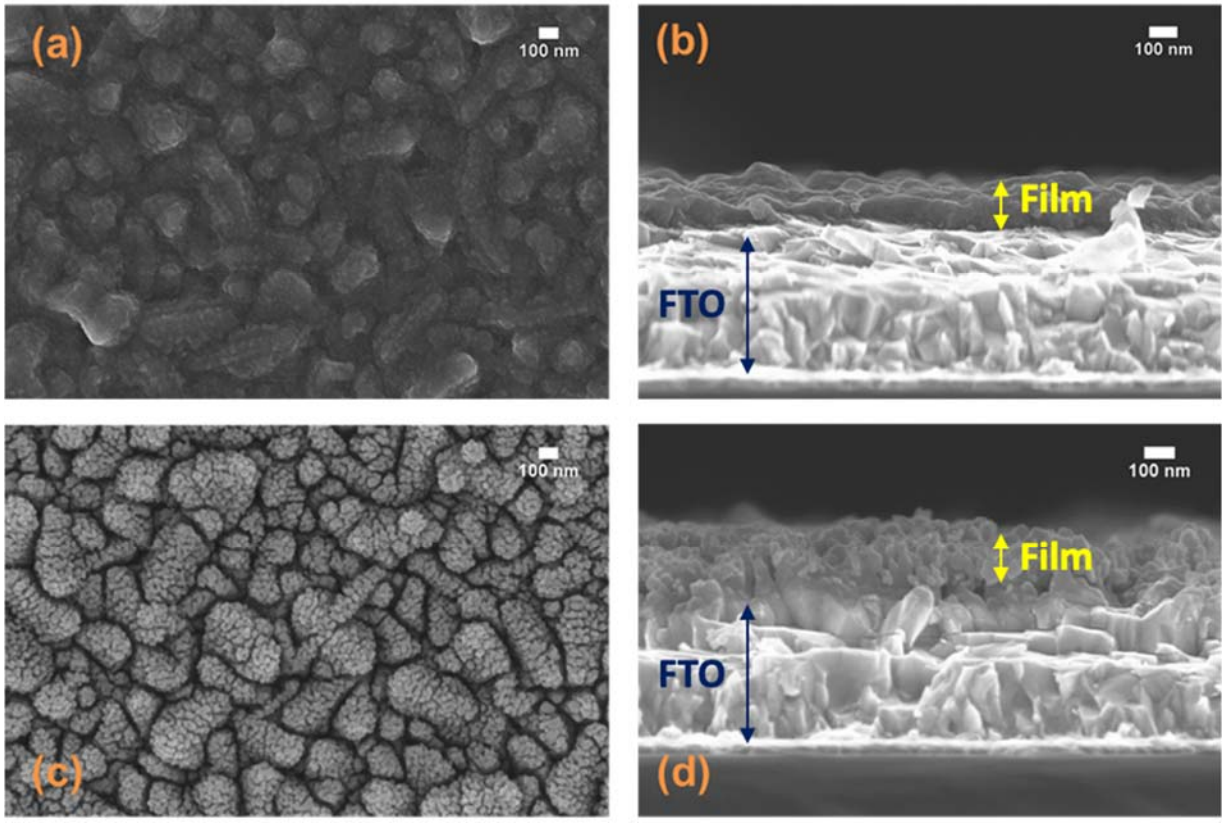

Figure 3: FESEM top view (a,c) and cross-sectional images (b,d) of films deposited under vacuum (a,b) and oxygen (c,d) atmosphere, respectively. Both films were annealed at 650°C for 2h in air.

The surface morphology of the films was analyzed using Field Emission Scanning Electron Microscopy (FESEM) as shown in Figure 3. Films deposited under vacuum were composed of a network of small nanoparticles grown on the substrate (Figure 3a). The cross-sectional image in Figure 3b shows a compact film with a thickness of around 100 nm. This is in contrast to thin films grown in an oxygen atmosphere (Figure 3c) which exhibits a porous surface with bigger grains, of around 30-40 nm diameter, conformally covering the FTO grains. The cross-sectional image, shown in Figure 3d demonstrates that the grains were stacked on FTO and the film had voids between the grains which increased its porosity. Due to the nucleation and growth of grains on the substrate, the film adhesion was strong. The findings in RBS measurements, as mentioned earlier in Figure 1, are consistent with such porous nature of films with possible pinholes. Energy Dispersive X-ray (EDX) analysis of the films (Figure S4, SI) clearly shows peaks

corresponding to both Fe and Ti in the films deposited in vacuum and under an oxygen atmosphere. The high Sn signal for both measurements is from the FTO layer underneath the films. It is unlikely that Sn has diffused from the FTO layer through the bulk of the semiconducting layers to the surface since the annealing temperature of the films was kept below 700°C[49].

To confirm the surface composition and the chemical states of the films deposited in an oxygen pressure of 9.7 x 10^{-2} mbar and vacuum (1.1 x 10^{-6} mbar), XPS measurements were performed. The survey spectra for the two films, presented in Figure S5a, indicates the presence of Fe, Ti, and O elements in the post-deposition annealed samples. A noticeable difference was the occurrence of Sn 3d peaks in the oxygen grown samples which were absent in the vacuum samples. A high-resolution scan of Sn 3d, as shown in Figure S5b, with the fitting of Sn $3d_{5/2}$ peaks for SnO_2 and SnF_2 at around 486.7 eV and 487.2 eV, respectively, indicates the presence of SnO_2 along with some parts of SnF_2. This suggests the exposure of the FTO grains to the surface in the porous oxygen grown films. It is to be noted that such exposure limits the performance of the photoanodes due to shunting of the back contact and electrolyte and can be prevented by a surface overlayer. The O 1s spectra shown in Figure S5c indicates the similar peak positions at around 530 eV for both samples assigned to lattice oxides. It also shows signals corresponding to hydroxides and other surface oxide species present with a slightly higher binding energy.

The Fe 2p high-resolution scan of the films along with the fitting following methodology presented earlier by Biesinger *et al* is shown in Figure 4a.[50] The Fe $2p_{3/2}$ region was fitted to a high spin sextet peak model for Fe^{3+} and pentet peak model for Fe^{2+} species. The spectra constitute the characteristic peaks of Fe $2p_{1/2}$ and Fe $2p_{3/2}$ centered at *ca.* 724.4 and 711 eV, respectively, which confirmed that Fe in both the films mainly existed as Fe^{3+}. For the Ti 2p spectrum shown in Figure 4b, the two standard peaks with binding energies of around 464.2 eV and 458.5 eV were attributed to Ti $2p_{1/2}$ and Ti $2p_{3/2}$, respectively, indicating Ti^{4+} in both the films.

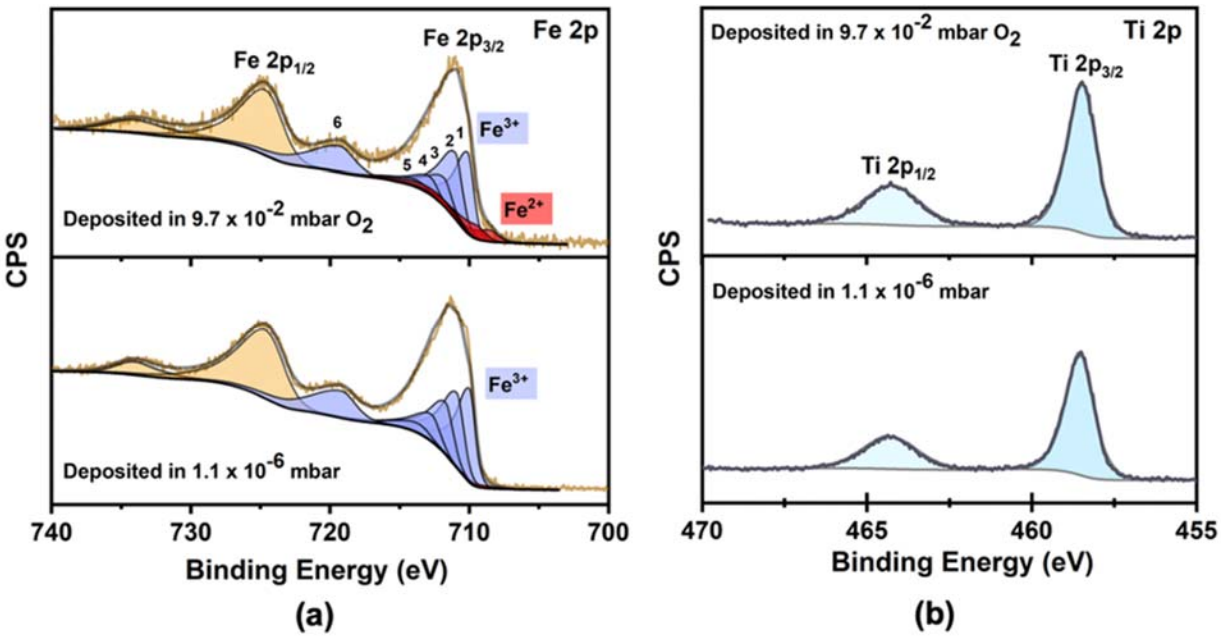

Figure 4: High-resolution XPS scans of the (a) Fe 2p and (b) Ti 2p region for films deposited in a vacuum (1.1 x 10^{-6} mbar) and oxygen atmosphere (9.7 x 10^{-2} mbar O_2)

The detailed fitting of Fe $2p_{3/2}$ peak, shown as violet peaks numbered 1 to 6, were used to quantify the Fe:Ti ratios on the surface or near-surface region of the films. It was determined that the films prepared under vacuum (1.1 x 10^{-6} mbar) were rich in iron showing an Fe:Ti ratio of ~ 3.3 while films deposited in oxygen pressure (9.7 x 10^{-2} mbar O_2) exhibited an Fe:Ti ratio of ~ 1. The spectra also indicated a higher presence of Fe^{2+} species (fitted as red peaks) with a ratio of Fe^{2+}:Fe^{3+} = 0.24 for the oxygen grown films as compared to vacuum grown films (around 0.04). These results can be correlated with the XRD findings where in vacuum grown films, the possibility of a hematite-type iron titanate of composition $Fe_{1.698}Ti_{0.228}O_3$, or Ti-alloyed Fe_2O_3 has been discussed. Such a phase present on the surface could be contributing to the orange color of the films. The Fe:Ti ratio of ~ 1 and higher Fe^{2+} content on the surface of oxygen grown films could also possibly point to the ilmenite-type composition $Fe^{2+}Ti^{4+}O_3$. These results suggest that in the bulk, the stoichiometry (Fe:Ti = 1.8 : 1) attained is independent of the background pressure whereas on the surface/near-surface region, overall Fe content (in Fe^{3+} state) is higher in the vacuum grown

samples whereas the amount of Fe^{2+} species on the surface is marginally higher in the oxygen grown samples.

Photoelectrochemical characterization

To evaluate the photoactivity of the Fe_2TiO_5 films fabricated by PLD, photoelectrochemical characterization was performed on samples using a 3-electrode configuration under chopped solar simulated light of AM1.5G in 1M NaOH electrolyte. It must be noted that all films were measured without any co-catalyst or passivating layer or a hole scavenger. As shown in Figure 5a, the photocurrent density shows higher values for electrodes deposited under the oxygen atmosphere (9.7×10^{-2} mbar O_2) than those deposited under vacuum (1.1×10^{-6} mbar). An onset potential of around 0.75V vs RHE is found from the chopped light plot (see Figure S6, SI) for the films grown in oxygen pressure. This is a negative shift in onset potential by 150 mV as compared to film grown in vacuum indicating better surface hole injection into the electrolyte. It must be noted that these films were illuminated via the substrate (i.e., backside illumination). A photocurrent of around 0.16 mA/cm^2 at 1.23 V vs RHE is observed for films grown in oxygen atmosphere as compared to 0.12 mA/cm^2 for samples deposited in vacuum.

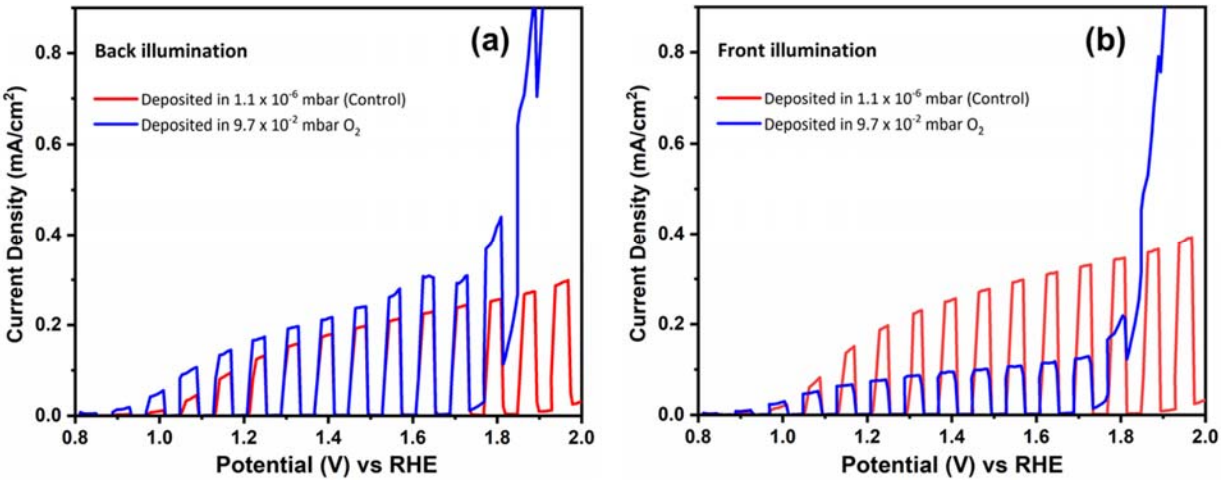

Figure 5: Photocurrent density vs applied bias curves for films deposited under vacuum (1.1×10^{-6} mbar) and oxygen atmosphere (9.7×10^{-2} mbar) (a) illuminated via the substrate (backside illumination) and (b) via the electrolyte (frontside illumination)

The photocurrent density under frontside illumination, as shown in Figure 5b, presents an interesting trend. When grown in an oxygen atmosphere, the films show smaller photocurrents than the ones grown in vacuum; this is opposite from the behavior of back-illuminated films. This could be due to the difference in their morphologies and composition gradients interconnected with different electron and hole mobilities in the films deposited under different oxygen background pressures. As reference, the photocurrent density curves for films grown in the different atmosphere under the backside and frontside illumination are shown in Figure S7, SI. The data in Figure S7 clearly show that for frontside illumination, the photocurrent depends more strongly on the deposition atmosphere than for backside illumination. One possible explanation for the pronounced decrease in photocurrent for the film deposited at higher oxygen pressures (for frontside illumination) is a lower electronic conductivity of the films. This can be explained by the improved crystalline quality and lower carrier density that is often found after annealing n-type metal oxides in an oxygen-rich atmosphere.[51-52] We also find a negative onset potential shift for films deposited in an oxygen atmosphere, both for frontside and backside illumination. This typically signifies a better hole injection at the semiconductor-electrolyte interface and is attributed to the higher porosity (i.e., internal surface area) of these films.

Films of different thicknesses were also fabricated and characterized for optimization. Thin films of thickness 50nm, 100 nm, and 200 nm were deposited in oxygen atmosphere (9.7×10^{-2} mbar) and their photoelectrochemical performances were evaluated as shown in Figure S8 (SI). It shows that 100 nm films gave the highest photocurrent density and IPCE values. Interestingly, this batch yielded a slightly higher photocurrent of 0.2 mA/cm^2 at 1.23 V vs RHE as compared to the ones presented earlier in Figure 5. We speculate that this might be due to the fluctuation of the plasma plume during PLD under these relatively high-pressure conditions, which can induce irregularities in the films and also influence their PEC performance. Nevertheless, the 100 nm films deposited under similar oxygen atmosphere (9.7×10^{-2} mbar) have been reproducible for different batches as shown in Figure S9(SI). In the following sections, the

optimized 100 nm films deposited under the oxygen atmosphere (9.7 x 10^{-2} mbar) and a fluence of 2.5 J/cm^2 will be used for further characterizations unless specified.

The photocurrent density of PLD grown films strikes a similarity with other reports where Fe_2TiO_5 has been used as the standalone photoanode without any overlayer or underlayer or cocatalyst. An *et al* presented the synthesis of Fe_2TiO_5 inverse opal (IO-250) photoanodes using polystyrene (PS) photonic crystals as templates which resulted in a photocurrent density of 0.05 mA/cm^2 at 1.23 V vs RHE under visible light irradiation in 1M NaOH electrolyte.[53] Courtin *et al* reported Fe_x-TiO_2 nanoheterostructured photoanodes fabricated via templated growth-based strategy.[19] The optimized $Fe_{0.2}$ -TiO_2 yielded a value of 0.15 mA/cm^2 at 1.23 V vs RHE which composed of a mixture of phases including Fe_2TiO_5, Fe_2O_3, and Fe-doped anatase. Wang et al demonstrated nanostructured Fe_2TiO_5 photoanodes prepared through electrospray technique which yielded 0.18 mA/cm^2 at 1.23 V vs RHE which further increased to 0.4 mA/cm^2 after surface F-modification.[54] Zhang et al showed highly ordered iron titanate (Fe_2TiO_5) nanotube array photoanodes which resulted in a relatively higher photocurrent density of around 0.34 mA/cm^2 at 1.23 V vs RHE which was further enhanced using triple modification techniques.[21] These reports demonstrate the feature that Fe_2TiO_5 photoanodes on its own have remained a lower-performing candidate as compared to other prominent oxides and would need further intrinsic modifications to prove their utility for the photoelectrochemical cell devices.

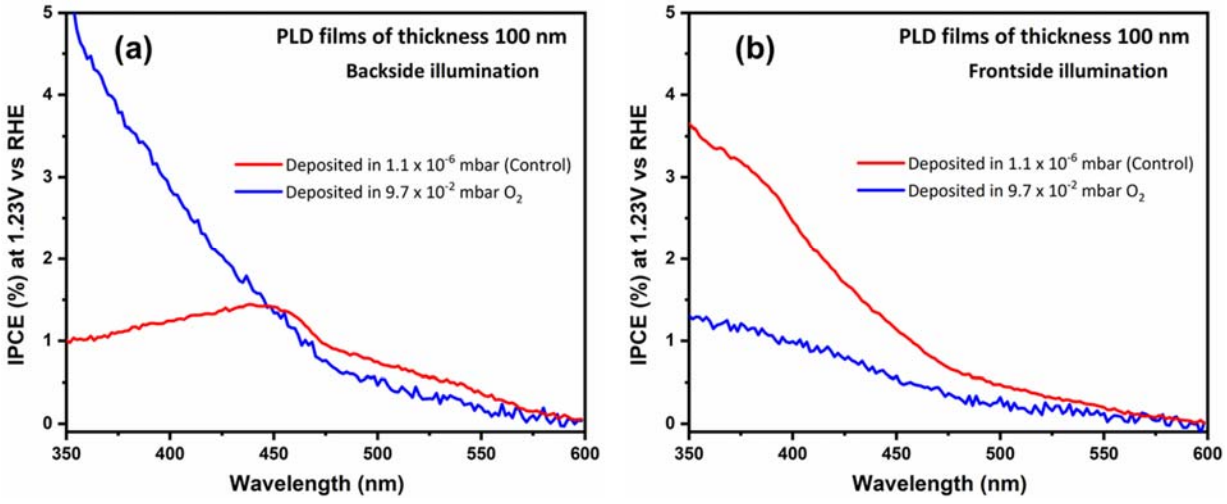

Figure 6: Incident photon to current efficiency (IPCE) curves at 1.23 V vs RHE, for films deposited at a pressure of 1.1 x 10^{-6} mbar and 9.7 x 10^{-2} mbar O_2 under (a) backside and, (b) frontside illumination

Figure 6 shows the incident photon-to-current efficiency (IPCE) as a function of incident light wavelength for photoanodes, measured at 1.23 V vs RHE in 1M NaOH electrolyte. For backside illumination (Figure 6a), the samples deposited under the oxygen atmosphere show an overall higher IPCE than the samples deposited under vacuum which corroborates the photocurrent density profile. The lower IPCE at shorter wavelengths for films grown in the vacuum can be explained by the fact that these films were more compact; this means that the photogenerated holes have to travel all the way through the 100 nm film before they reach the semiconductor/electrolyte interface. Hole transport is usually not very efficient in n-type semiconducting films, which explains the lower IPCE. The IPCE curves for films deposited at 1.1 x 10^{-6} mbar (compact film) and 9.7 x 10^{-2} mbar (porous film) show identical behavior in the wavelength range from 600 nm to 460 nm. This is because the absorption coefficient is much smaller at these wavelengths, which means that the light is homogeneously absorbed throughout the entire film and the distinction between carriers that have to travel long vs short distances becomes less pronounced.

IPCE under frontside illumination was also evaluated (as shown in Figure 6b) which showed an interesting variation. Films grown under vacuum showed the highest frontside current among all the variations. For films grown in an oxygen atmosphere, the frontside photocurrent was much lower than the one in the backside configuration. Following the discussion above, we attribute this to the lower electronic conductivity and more porous morphology of the films deposited in an oxygen atmosphere, which hinders electron transport from the front to the back contact of the film.

Stability measurement

To access the stability of the photoanodes, amperometry measurements were performed. Current density vs time curves at a fixed applied potential of 1.23 V vs RHE, as shown in Figure 7a, demonstrate the drop in current density from 0.175 mA/cm^2 to around 0.13 mA/cm^2 in around 45 min, which regains back to

0.16 mA/cm^2 after the light is turned off and on, and further stabilize again to around 0.13 mA/cm^2. Based on this behavior, we attribute the decrease in photocurrent to acidification of the films at the electrolyte/electrode interface. The recovery of the signal after switching the light off and on again shows the absence of any electrochemical or physical instability in the films under illumination. The electrochemical stability was further checked by comparing the linear sweep curves before and after 1h stability measurement, as shown in Figure 7b. It shows that the current profile remained similar after prolonged illumination and hence photoanodes seem to be stable. This should be further pursued with a longer measurement up to at least 100h. To investigate if the linear sweep PEC measurements induced any structural or morphological changes, XRD and FESEM measurements were performed before and after the PEC measurement of oxygen grown samples as shown in Figure S10. The XRD peaks did not show any shift and the morphology remained similar even after PEC measurement reaffirming the electrochemical and mechanical stability of oxygen grown thin films.

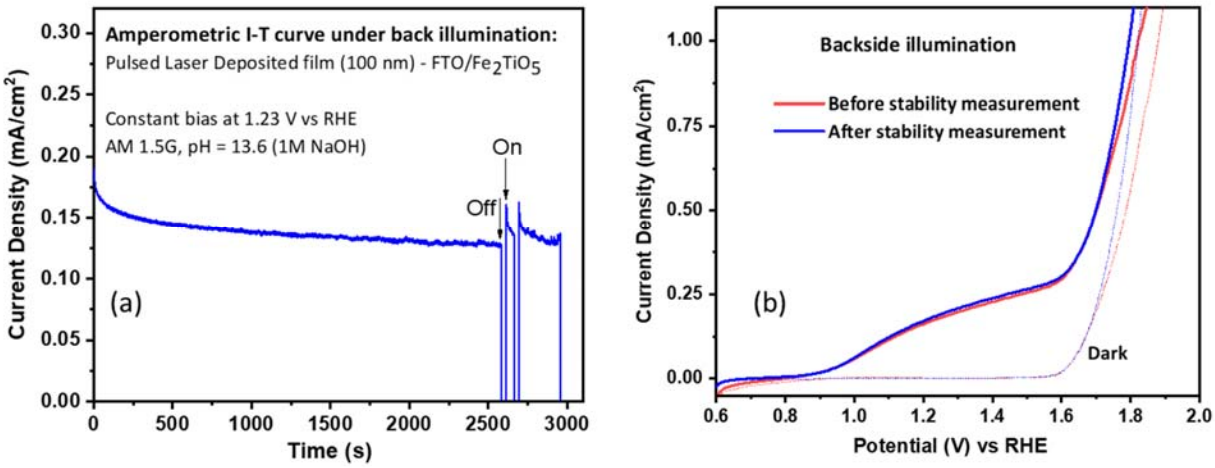

Figure 7: (a) Amperometric curve for stability, and (b) Current density – potential curve before and after the stability measurement for FTO/Fe_2TiO_5 photoanodes deposited in 9.7 x 10^{-2} mbar oxygen pressure

In sum, the pure phase films grown through PLD in oxygen atmosphere showed good stability in 1M NaOH electrolyte, but the performance was still lower as compared to other prominent photoanodes like Fe_2O_3,

WO_3, $BiVO_4$, etc.[10] We believe that the low performance of Fe_2TiO_5 photoanodes mostly emanates from their low absorption coefficient and low bulk charge carrier conductivity. The low absorption by the crystalline Fe_2TiO_5 phase (P4) is evident in Figure 2b. Whereas, crude evidence of low conductivity can be observed from the PEC curves (in Figure 5) where increasing the photocurrent density saturates shortly after achieving photocurrent onset, due to higher charge transfer resistance.

For the subsequent study, the low absorption can be enhanced by fabricating nanostructures which can exhibit light trapping effects and enlarged surface area for better charge separation. Most recently, Chen *et al* demonstrated Indium–tin-oxide/Fe_2TiO_5 hybrid nanocone arrays which significantly improved photocurrent generation up to 31 times as compared to films deposited on planar substrates.[55] The ITO nanocone platform enhanced the overall solar light absorption and the surface area leading to improved performance. Improvement in base Fe_2TiO_5 photoanodes can yield even higher performance after further optimization. Another possibility is by improving their n-type conductivity by elemental doping with multivalent elements. Lately, Lee *et al* demonstrated their novel synthesis techniques involving metal-catechol complexes and subsequently doping Fe_2TiO_5 with Sn^{+4} ions.[56] They concluded that Sn dopants serve as donors at Fe sites and increase the majority carrier density leading to improvement in the photoelectrochemical performance of Fe_2TiO_5 photoanodes. Additionally, the present grain size of around 30-40 nm in the oxygen grown films can be further increased by tuning synthesis conditions. As shown for other metal oxides like Fe_2O_3, bigger grain size results in a smaller number of grain boundaries leading to a smaller number of recombination centers for photogenerated electron-hole pairs. Hence, systematic research into tuning the aforementioned intrinsic properties could lead the scientific community towards the development of Fe_2TiO_5 photoanodes which would also prove beneficial when coupling them as a window material on other complementary oxides.

CONCLUSIONS

In conclusion, preferentially oriented crystalline Fe_2TiO_5 thin films were synthesized using the Pulsed Laser Deposition technique (PLD). Films deposited on FTO substrates were tuned by altering the oxygen pressure during the deposition. Films grown in vacuum atmosphere (1.1×10^{-6} mbar) were compact but showed poor crystallinity, whereas films deposited under 9.7×10^{-2} mbar oxygen pressure crystallized in the orthorhombic Fe_2TiO_5 pseudobrookite phase after post-deposition annealing at 650°C for 2 hours in the air. These films possessed a long-range order with (101) oriented grains, as clearly observed by X-ray diffractogram. Optimized films demonstrated 40-50 nm grains uniformly dispersed on FTO grains in a nanoporous network. Photoelectrochemical characterization of thin films grown under oxygen atmosphere (9.7×10^{-2} mbar) yielded a cathodic shift in onset potential by 150 mV and a higher photocurrent density of around 0.16 mA/cm^2 at 1.23 V vs RHE as compared to the film grown under vacuum (0.12 mA/cm^2) under backside illumination. Since the anisotropic films were deposited on polycrystalline FTO substrates, it opens up the avenue for further research on Fe_2TiO_5 and similar multinary metal oxide photoanodes, fabricated by pulsed laser deposition. It also offers an opportunity to couple these crystalline films with complementary metal oxides grown via PLD, especially bottom absorbers, to yield higher efficiency photoelectrode systems.

ASSOCIATED CONTENT

Supporting Information

The supporting information includes schematic representation of PLD deposition, details about target, absorption coefficient, Tauc plots, EDX measurements, XPS survey, Sn 3d, and O1s scans, current density vs potential curve for onset potential, IPCE curves along with reproducibility plot and XRD/FESEM data for before and after PEC measurement.

AUTHOR INFORMATION

Corresponding Authors:

*E-mail for P.S.B.: prince.bassi@helmholtz-berlin.de; mail.princeb@gmail.com

*E-Mail for S.F.: fiechter@helmholtz-berlin.de

Author Contributions: The manuscript was written through contributions of all authors. All authors have given approval to the final version of the manuscript.

Notes: The authors declare no competing financial interest.

ACKNOWLEDGMENTS

S.F. and P.S.B. would like to thank Deutsche Forschungsgemeinschaft (DFG) for financial support through the priority program SPP1613 entitled "Fuels Produced Regeneratively through Light-Driven Water Splitting: Clarification of the Elemental Processes Involved and Prospects for Implementation in Technological Concepts". The authors are grateful to Dr. Ronen Gottesman and Mr. Karsten Harbauer for the technical support and fruitful discussions about PLD processes in both theory and experiment. In addition, support of Mr. René Heller from the Ion Beam Center at the Helmholtz - Zentrum Dresden-Rossendorf performing RBS measurements is gratefully acknowledged. The authors would also like to thank Mr. Bennet Wildenauer for his help in the preparation of the PLD target. Also, part of the work was funded by the Volkswagen Foundation.

References

1. Creutzig, F.; Agoston, P.; Goldschmidt, J. C.; Luderer, G.; Nemet, G.; Pietzcker, R. C. The Underestimated Potential of Solar Energy to Mitigate Climate Change. *Nature Energy* **2017**, *2*, 17140.
2. Lewis, N. S.; Nocera, D. G. Powering the Planet: Chemical Challenges in Solar Energy Utilization. *P Natl Acad Sci USA* **2006**, *103*, 15729-15735.
3. Bassi, P. S.; Gurudayal; Wong, L. H.; Barber, J. Iron Based Photoanodes for Solar Fuel Production. *Phys Chem Chem Phys* **2014**, *16*, 11834-11842.

4. He, Y. M.; Hamann, T.; Wang, D. W. Thin Film Photoelectrodes for Solar Water Splitting. *Chemical Society Reviews* **2019**, *48*, 2182-2215.
5. Moniz, S. J. A.; Shevlin, S. A.; Martin, D. J.; Guo, Z.-X.; Tang, J. Visible-Light Driven Heterojunction Photocatalysts for Water Splitting – a Critical Review. *Energy & Environmental Science* **2015**, *8*, 731-759.
6. Butler, M. A. Photoelectrolysis and Physical-Properties of Semiconducting Electrode WO_3. *J Appl Phys* **1977**, *48*, 1914-1920.
7. Santato, C.; Ulmann, M.; Augustynski, J. Photoelectrochemical Properties of Nanostructured Tungsten Trioxide Films. *J. Phys. Chem. B* **2001**, *105*, 936-940.
8. Sivula, K.; Le Formal, F.; Grätzel, M. Solar Water Splitting: Progress Using Hematite (α-Fe_2O_3) Photoelectrodes. *ChemSusChem* **2011**, *4*, 432-449.
9. Sivula, K. Chapter 6 Emerging Semiconductor Oxides for Direct Solar Water Splitting. In *Advances in Photoelectrochemical Water Splitting: Theory, Experiment and Systems Analysis*, The Royal Society of Chemistry: 2018; pp 163-182.
10. Lee, D. K.; Lee, D.; Lumley, M. A.; Choi, K. S. Progress on Ternary Oxide-Based Photoanodes for Use in Photoelectrochemical Cells for Solar Water Splitting. *Chemical Society Reviews* **2019**, *48*, 2126-2157.
11. Kim, M.; Lee, B.; Ju, H.; Kim, J. Y.; Kim, J.; Lee, S. W. Oxygen-Vacancy-Introduced $BaSnO_{3-\delta}$ Photoanodes with Tunable Band Structures for Efficient Solar-Driven Water Splitting. *Advanced Materials* **2019**, *31*, 1903316.
12. Kölbach, M.; Pereira, I. J.; Harbauer, K.; Plate, P.; Höflich, K.; Berglund, S. P.; Friedrich, D.; van de Krol, R.; Abdi, F. F. Revealing the Performance-Limiting Factors in α-$SnWO_4$ Photoanodes for Solar Water Splitting. *Chemistry of Materials* **2018**, *30*, 8322-8331.
13. Park, Y.; McDonald, K. J.; Choi, K.-S. Progress in Bismuth Vanadate Photoanodes for Use in Solar Water Oxidation. *Chemical Society Reviews* **2013**, *42*, 2321-2337.
14. Song, A.; Chemseddine, A.; Ahmet, I. Y.; Bogdanoff, P.; Friedrich, D.; Abdi, F. F.; Berglund, S. P.; van de Krol, R. Evaluation of Copper Vanadate (B-$Cu_2V_2O_7$) as a Photoanode Material for Photoelectrochemical Water Oxidation. *Chemistry of Materials* **2020**.
15. Niishiro, R.; Takano, Y.; Jia, Q.; Yamaguchi, M.; Iwase, A.; Kuang, Y.; Minegishi, T.; Yamada, T.; Domen, K.; Kudo, A. A CoO_x-Modified $SnNb_2O_6$ Photoelectrode for Highly Efficient Oxygen Evolution from Water. *Chemical Communications* **2017**, *53*, 629-632.
16. Kment, S.; Riboni, F.; Pausova, S.; Wang, L.; Wang, L.; Han, H.; Hubicka, Z.; Krysa, J.; Schmuki, P.; Zboril, R. Photoanodes Based on TiO_2 and α-Fe_2O_3 for Solar Water Splitting – Superior Role of 1D Nanoarchitectures and of Combined Heterostructures. *Chemical Society Reviews* **2017**, *46*, 3716-3769.
17. Gurudayal; Bassi, P. S.; Sritharan, T.; Wong, L. H. Recent Progress in Iron Oxide Based Photoanodes for Solar Water Splitting. *Journal of Physics D: Applied Physics* **2018**, *51*, 473002.
18. Bassi, P. S.; Chiam, S. Y.; Gurudayal; Barber, J.; Wong, L. H. Hydrothermal Grown Nanoporous Iron Based Titanate, Fe_2TiO_5 for Light Driven Water Splitting. *ACS Applied Materials & Interfaces* **2014**, *6*, 22490-22495.
19. Courtin, E.; Baldinozzi, G.; Sougrati, M. T.; Stievano, L.; Sanchez, C.; Laberty-Robert, C. New Fe_2TiO_5-based Nanoheterostructured Mesoporous Photoanodes with Improved Visible Light Photoresponses. *J Mater Chem A* **2014**, *2*, 6567-6577.
20. An, X.; Lan, H.; Liu, R.; Liu, H.; Qu, J. Light Absorption Modulation of Novel Fe_2TiO_5 Inverse Opals for Photoelectrochemical Water Splitting. *New Journal of Chemistry* **2017**, *41*, 7966-7971.
21. Zhang, H.; Kim, J. H.; Kim, J. H.; Lee, J. S. Engineering Highly Ordered Iron Titanate Nanotube Array Photoanodes for Enhanced Solar Water Splitting Activity. *Advanced Functional Materials* **2017**, *27*, 1702428.
22. Lou, Z. R.; Li, Y. G.; Song, H.; Ye, Z. Z.; Zhu, L. P. Fabrication of Fe_2TiO_5/TiO_2 Nanoheterostructures with Enhanced Visible-Light Photocatalytic Activity. *RSC Adv* **2016**, *6*, 45343-45348.

23. Deng, Y. X.; Xing, M. Y.; Zhang, J. L. An Advanced $TiO_2/Fe_2TiO_5/Fe_2O_3$ Triple-Heterojunction with Enhanced and Stable Visible-Light-Driven Fenton Reaction for the Removal of Organic Pollutants. *Appl Catal B-Environ* **2017**, *211*, 157-166.
24. Waqas, M.; Wei, Y. Z.; Mao, D.; Qi, J.; Yang, Y.; Wang, B.; Wang, D. Multi-Shelled TiO_2/Fe_2TiO_5 Heterostructured Hollow Microspheres for Enhanced Solar Water Oxidation. *Nano Res* **2017**, *10*, 3920-3928.
25. Xiong, K.; Wang, K. Z.; Chen, L.; Wang, X. Q.; Fan, Q. B.; Courtois, J.; Liu, Y. L.; Tuo, X. G.; Yan, M. H. Heterostructured $ZnFe_2O_4/Fe_2TiO_5/TiO_2$ Composite Nanotube Arrays with an Improved Photocatalysis Degradation Efficiency under Simulated Sunlight Irradiation. *Nano-Micro Lett* **2018**, *10*.
26. Liu, Q. H., et al. Aligned Fe_2TiO_5-Containing Nanotube Arrays with Low Onset Potential for Visible-Light Water Oxidation. *Nat Commun* **2014**, *5*.
27. Deng, J. J.; Lv, X. X.; Liu, J. Y.; Zhang, H.; Nie, K. Q.; Hong, C. H.; Wang, J. O.; Sun, X. H.; Zhong, J.; Lee, S. T. Thin-Layer Fe_2TiO_5 on Hematite for Efficient Solar Water Oxidation. *ACS Nano* **2015**, *9*, 5348-5356.
28. Feng, X.; Chen, Y.; Qin, Z.; Wang, M.; Guo, L. Facile Fabrication of Sandwich Structured WO_3 Nanoplate Arrays for Efficient Photoelectrochemical Water Splitting. *ACS Applied Materials & Interfaces* **2016**, *8*, 18089-18096.
29. Deng, J. J.; Lv, X. X.; Nie, K. Q.; Lv, X. L.; Sun, X. H.; Zhong, J. Lowering the Onset Potential of Fe_2TiO_5/Fe_2O_3 Photoanodes by Interface Structures: F- and Rh-Based Treatments. *ACS Catal* **2017**, *7*, 4062-4069.
30. Lv, X. L.; Nie, K. Q.; Lan, H. W.; Li, X.; Li, Y. Y.; Sun, X. H.; Zhong, J.; Lee, S. T. Fe_2TiO_5-Incorporated Hematite with Surface P-Modification for High-Efficiency Solar Water Splitting. *Nano Energy* **2017**, *32*, 526-532.
31. Deng, J. J.; Lv, X. X.; Zhong, J. Photocharged Fe_2TiO_5/Fe_2O_3 Photoanode for Enhanced Photoelectrochemical Water Oxidation. *J Phys Chem C* **2018**, *122*, 29268-29273.
32. Bassi, P. S.; Antony, R. P.; Boix, P. P.; Fang, Y. N.; Barber, J.; Wong, L. H. Crystalline Fe_2O_3/Fe_2TiO_5 Heterojunction Nanorods with Efficient Charge Separation and Hole Injection as Photoanode for Solar Water Oxidation. *Nano Energy* **2016**, *22*, 310-318.
33. Lowndes, D. H.; Geohegan, D. B.; Puretzky, A. A.; Norton, D. P.; Rouleau, C. M. Synthesis of Novel Thin-Film Materials by Pulsed Laser Deposition. *Science* **1996**, *273*, 898-903.
34. Ma, C. C., C. Pulsed Laser Deposition for Complex Oxide Thin Film and Nanostructure. In *Advanced Nano Deposition Methods*, Lin, Y. C., X., Ed. Chemical Industry Press: 2016; pp 1-31.
35. Osada, M.; Nishio, K.; Hwang, H. Y.; Hikita, Y. Synthesis and Electronic Properties of Fe_2TiO_5 Epitaxial Thin Films. *Apl Mater* **2018**, *6*.
36. Ngo, H. D.; Ngo, T. D.; Tamanai, A.; Chen, K.; Cuong, N. T.; Handegard, O. S.; Pucci, A.; Umezawa, N.; Nabatame, T.; Nagao, T. Structure and Optical Properties of Sputter Deposited Pseudobrookite Fe_2TiO_5 Thin Films. *Crystengcomm* **2019**, *21*, 34-40.
37. Peerakiatkhajohn, P.; Yun, J. H.; Chen, H.; Lyu, M.; Butburee, T.; Wang, L. Stable Hematite Nanosheet Photoanodes for Enhanced Photoelectrochemical Water Splitting. *Advanced Materials* **2016**, *28*, 6405-6410.
38. Amoruso, S.; Sambri, A.; Wang, X. Plume Expansion Dynamics During Laser Ablation of Manganates in Oxygen Atmosphere. *Appl Surf Sci* **2007**, *253*, 7696-7701.
39. Canulescu, S.; Papadopoulou, E. L.; Anglos, D.; Lippert, T.; Schneider, C. W.; Wokaun, A. Mechanisms of the Laser Plume Expansion During the Ablation of $LiMn_2O_4$. *J Appl Phys* **2009**, *105*.
40. Kölbach, M.; Harbauer, K.; Ellmer, K.; van de Krol, R. Elucidating the Pulsed Laser Deposition Process of $BiVO_4$ Photoelectrodes for Solar Water Splitting. *J Phys Chem C* **2020**, *124*, 4438-4447.
41. Di Fonzo, F.; Tonini, D.; Li Bassi, A.; Casari, C. S.; Beghi, M. G.; Bottani, C. E.; Gastaldi, D.; Vena, P.; Contro, R. Growth Regimes in Pulsed Laser Deposition of Aluminum Oxide Films. *Applied Physics A* **2008**, *93*, 765-769.

42. Infortuna, A.; Harvey, A. S.; Gauckler, L. J. Microstructures of CGO and YSZ Thin Films by Pulsed Laser Deposition. *Advanced Functional Materials* **2008**, *18*, 127-135.
43. Groenen, R.; Smit, J.; Orsel, K.; Vailionis, A.; Bastiaens, B.; Huijben, M.; Boller, K.; Rijnders, G.; Koster, G. Research Update: Stoichiometry Controlled Oxide Thin Film Growth by Pulsed Laser Deposition. *Apl Mater* **2015**, *3*.
44. Yang, J.; Hou, J.; Niu, Y.; Li, W.; Yi, F.; Liu, S.; Li, G.; Xu, M. Improved Cycle Capability of Titanium-Doped Fe_2O_3 Anode Material for Li-Ion Batteries. *Journal of Alloys and Compounds* **2017**, *722*, 414-419.
45. Guo, W. Q.; Malus, S.; Ryan, D. H.; Altounian, Z. Crystal Structure and Cation Distributions in the $FeTi_2O_5$- Fe_2TiO_5 Solid Solution Series. *Journal of Physics: Condensed Matter* **1999**, *11*, 6337-6346.
46. Seitz, G.; Penin, N.; Decoux, L.; Wattiaux, A.; Duttine, M.; Gaudon, M. Near the Ferric Pseudobrookite Composition (Fe_2TiO_5). *Inorganic Chemistry* **2016**, *55*, 2499-2507.
47. Yaghoubi, H.; Li, Z.; Chen, Y.; Ngo, H. T.; Bhethanabotla, V. R.; Joseph, B.; Ma, S. Q.; Schlaf, R.; Takshi, A. Toward a Visible Light-Driven Photocatalyst: The Effect of Midgap-States-Induced Energy Gap of Undoped TiO_2 Nanoparticles. *ACS Catal* **2015**, *5*, 327-335.
48. Wang, J.; Wang, Z.; Huang, B.; Ma, Y.; Liu, Y.; Qin, X.; Zhang, X.; Dai, Y. Oxygen Vacancy Induced Band-Gap Narrowing and Enhanced Visible Light Photocatalytic Activity of ZnO. *ACS applied materials & interfaces* **2012**, *4*, 4024-30.
49. Ling, Y.; Wang, G.; Wheeler, D. A.; Zhang, J. Z.; Li, Y. Sn-Doped Hematite Nanostructures for Photoelectrochemical Water Splitting. *Nano Letters* **2011**, *11*, 2119-2125.
50. Biesinger, M. C.; Payne, B. P.; Grosvenor, A. P.; Lau, L. W. M.; Gerson, A. R.; Smart, R. S. C. Resolving Surface Chemical States in Xps Analysis of First Row Transition Metals, Oxides and Hydroxides: Cr, Mn, Fe, Co and Ni. *Appl Surf Sci* **2011**, *257*, 2717-2730.
51. Ke, C.; Yang, Z.; Pan, J. S.; Zhu, W.; Wang, L. Annealing Induced Anomalous Electrical Transport Behavior in SnO_2 Thin Films Prepared by Pulsed Laser Deposition. *Appl Phys Lett* **2010**, *97*.
52. Wang, C. M.; Huang, C. C.; Kuo, J. C.; Sahu, D. R.; Huang, J. L. Effect of Annealing Temperature and Oxygen Flow in the Properties of Ion Beam Sputtered SnO_{2-X} Thin Films. *Materials* **2015**, *8*, 5289-5297.
53. An, X. Q.; Lan, H. C.; Liu, R. P.; Liu, H. J.; Qu, J. H. Light Absorption Modulation of Novel Fe_2TiO_5 Inverse Opals for Photoelectrochemical Water Splitting. *New Journal of Chemistry* **2017**, *41*, 7966-7971.
54. Wang, M.; Wu, X.; Huang, K.; Sun, Y.; Zhang, Y.; Zhang, H.; He, J.; Chen, H.; Ding, J.; Feng, S. Enhanced Solar Water-Splitting Activity of Novel Nanostructured Fe_2TiO_5 Photoanode by Electrospray and Surface F-Modification. *Nanoscale* **2018**, *10*, 6678-6683.
55. Chen, K.; Dao, T. D.; Ngo, T. D.; Ngo, H. D.; Tamanai, A.; Ishii, S.; Li, X.; Misawa, H.; Nagao, T. Enhanced Photocurrent Generation from Indium–Tin-Oxide/Fe_2TiO_5 Hybrid Nanocone Arrays. *Nano Energy* **2020**, *76*, 104965.
56. Lee, D.; Baltazar, V. U.; Smart, T. J.; Ping, Y.; Choi, K. S. Electrochemical Oxidation of Metal–Catechol Complexes as a New Synthesis Route to the High-Quality Ternary Photoelectrodes: A Case Study of Fe_2TiO_5 Photoanodes. *ACS Applied Materials & Interfaces* **2020**, *12*, 29275-29284.

Pulsed Laser Deposited Fe_2TiO_5 Photoanodes for Photoelectrochemical Water Oxidation

Prince Saurabh Bassi[†]*, Fanxing Xi[†], Moritz Kölbach[†], Rene Gunder[§], Ibbi Ahmet[†], Roel van de Krol[†‡], Sebastian Fiechter[†]*

For Table of Contents (TOC) Graphic